Catalysis Surveys from Asia (2019) 23:210–218
https://doi.org/10.1007/s10563-019-09272-6

Influence of MnO_2 Morphology on the Catalytic Performance of Ag/MnO_2 for the HCHO Oxidation

Suhong Lu[1] · **Qinyu Zhu**[1] · **Yaxin Dong**[1] · **Yiming Zheng**[1] · **Xue Wang**[1] · **Kelun Li**[2] · **Fenglin Huang**[1] · **Bo Peng**[1] · **Yuliang Chen**[1]

Abstract

A series of Ag/MnO_2 catalysts employing MnO_2 nanorods (MnO_2-*r*) and nanoparticles (MnO_2-*n*) as the supports were prepared by conventional incipient wetness impregnation. Their structures had been characterized by BET, SEM, TEM, XRD, H_2-TPR, O_2-TPD and XPS. The catalytic activities in HCHO oxidation had also been investigated. The results showed that MnO_2-*r* and MnO_2-*n* exhibited different reducibility and surface active oxygen. Ag/MnO_2-*r* performed better reducibility and more surface active oxygen than that of Ag/MnO_2-*n*. It had observed that Ag/MnO_2-*r* could achieve complete oxidation of HCHO at 80 °C, due to the low-temperature reducibility and abundant surface active oxygen. Meanwhile, the Ag/MnO_2-*r* catalyst exhibited good stability.

Keywords Formaldehyde · Catalytic oxidation · Ag · Morphology · MnO_2

1 Introduction

Formaldehyde (HCHO) has been considered as a typical pollutant to the atmosphere and human health, which is mainly released from consumer products and building/furnishing materials [1]. Long-term exposure to indoor air containing even very low concentrations of HCHO may induce a variety of diseases, such as respiratory, skin irritation, nasal tumors, irritation to eyes and so on [2]. Thus, it is urgent to reduce the indoor HCHO emission in order to meet the strict environmental regulations.

So far, considerable technologies have been made to eliminate HCHO, including adsorption, photo-catalysis, plasma technology and catalytic oxidation methods [3]. Among them, catalytic oxidation of HCHO has been recognized as a promising technique, due to its high efficiency, low temperature, simple equipment and no secondary pollutant [4]. Therefore, it is the key to develop novel catalyst with efficient activity for the catalytic oxidation of HCHO at low temperature.

For decades, the conventional catalysts mainly include the supported noble metal catalysts (Pt, Pd and Au) [5–7] and transition metal oxide catalysts (MnO_2, Co_3O_4 and CeO_2) [8–10]. Especially, it has been reported that supported Pt catalyst can obtain complete conversion of HCHO at room temperature [5, 11, 12]. However, the high price of precious metals limits their widespread applications. Transition metal oxide catalysts are very cheap, but complete oxidation of HCHO is usually achieved at high temperature (> 100 °C). Thus, it is significant and urgent to exploit efficient and low cost catalysts. It has observed that supported Ag catalysts perform some outstanding ability in the reaction of HCHO oxidation [13, 14]. Therefore, Ag may be a promising substitute for catalytic oxidation of HCHO.

Manganese oxides have been greatly considered as promising, inexpensive and nontoxic materials in environmental catalysts, used in HCHO oxidation [15]. Bai et al. [16] prepared three dimensional ordered mesoporous MnO_2, which obtained complete oxidation of HCHO at 130 °C. Similar catalytic activity over mesoporous silica-confined manganese oxide was also reported by Averlant [17]. It is interesting that manganese oxides with different morphology have been widely applied as catalysts and shown exciting performance. Shi et al. [18] claimed that

---

✉ Suhong Lu
lusuhong@xsyu.edu.cn

[1] College of Chemistry and Chemical Engineering, Xi'an Shiyou University, Xi'an 710065, China

[2] Shaanxi Coal and Chemical Technology Institute Co., Ltd, Xi'an 710070, China

rod-like tetragonal α-MnO_2 showed good catalytic performance for the total oxidation of toluene. Liang et al. [19] pointed out the MnO_2 nanorods exhibited high activity for CO oxidation. To our knowledge, there have so far been rare studies on the catalytic application of MnO_2 with different morphology for the catalytic oxidation of HCHO.

In this work, the MnO_2 nanorods and MnO_2 nanoparticles were successfully synthesized and as supporters loaded a small amount of Ag. The influence of MnO_2 morphology on the catalytic performance of Ag/MnO_2 for HCHO oxidation have been revealed by BET, SEM, TEM, XRD, H_2-TPR, O_2-TPD and XPS. The effect of the different morphologies of the MnO_2 on HCHO oxidation was investigated. It was found that Ag/MnO_2 nanorods performed extremely high catalytic activity and 100% conversion of HCHO was obtained at temperature as low as 80 °C.

2 Experimental

2.1 Catalyst Preparation

The MnO_2 nanorods were prepared using the hydrothermal method, which was similar to the previous report [18]. Typically, for the case of MnO_2 nanorods (denoted as MnO_2-*r*), 16 mmol of $KMnO_4$ and 6 mmol of $MnSO_4$ precursor were dissolved in 160 mL of deionized water, and stirred for 1 h. And then, the mixture was charged into a Tefon-lined autoclave with a capacity of 200 mL, tightly sealed and hydrothermally treated at 160 °C for 12 h. After cooling, the resulting precipitate was collected by filtration, washed with deionized water and dried at 60 °C for 24 h. The acquired powder was calcined in muffle oven at 300 °C for 4 h with a heating rate of 1 °C min^{-1}, thus obtaining the final MnO_2-*r*.

The MnO_2 nanoparticles (designed as MnO_2-*n*) were synthesized by the water-bathing method. Briefly, 4 mmol of $KMnO_4$ was dissolved in 80 mL of deionized water, and 4 mL of 98 wt % H_2SO_4 solution was dropped into the $KMnO_4$ solution under vigorously stirring. After that, a piece of copper plate (2 cm × 8 cm) was added to the mixed solution and was water-bathed at 60 °C for 8 h [20].

Ag/MnO_2-*r* and Ag/MnO_2-*n* catalysts were synthesized by conventional wetness incipient impregnation method employing prepared MnO_2-*r* or MnO_2-*n* as the support. In the typical method, 1 g MnO_2-*r* or MnO_2-*n* was dispersed in 30 mL deionized water with vigorous stirring for 30 min and the desired amount of $AgNO_3$ solution was added dropwise. After that, the suspension was continuously stirred at 30 °C for 24 h and evaporated at 80 °C. The obtained powder was dried at 80 °C overnight. The amount of Ag in the final catalyst was 0.1 wt %, which was measured via ICP-AES.

2.2 Characterization

Nitrogen adsorption and desorption isotherms were acquired on a micromeritics apparatus (ASAP2020HD88). All samples were outgassed under vacuum at 250 °C for 4 h prior to analysis. The specific surface areas were computed by applying the Brunauer–Emmett–Teller (BET). The pore size distribution was estimated from the desorption branch of the isotherms using the BJH model.

The morphology of the product was characterized by scanning electron microscope (SEM, America FET Quanta 600 FEG). Transmission electron microscope (TEM) was obtained on the Tecnai G2 F20 apparatus.

Powder X-ray diffraction (XRD) measurements of the catalysts were recorded on a Panalytical Empyrean X-ray diffractometer with Cu-Ka radiation ($\lambda = 0.154{,}056$ nm) at 40 kV and 30 mA and the data were recorded at a scanning speed of 2° min^{-1} from 10.0° to 80.0°.

The temperature programmed reduction (H_2-TPR) was conducted with a thermal conductivity detector (TCD) connected to a flow-control system and a programmed heating unit. Before the H_2-TPR analysis, the samples were treated with 21 vol% O_2/N_2 flow (30 mL min^{-1}) at 300 °C for 1 h. About 50 mg of catalyst was used in each measurement. The H_2-TPR was performed by heating the catalysts from approximately 50 to 650 °C in a 10 vol% H_2/N_2 mixture with a flow rate of 60 mL min^{-1}.

Oxygen temperature-programmed desorption (O_2-TPD) tests were performed on the same instrument with H_2-TPR. Prior to each run, 60 mg of sample was pretreated under 21 vol% O_2/N_2 flow (30 mL min^{-1}) at the temperature of 300 °C for 1 h, and then reduced in a stream of 10 vol% H_2/N_2 flow at 200 °C for 1 h. Subsequently, the He gas was swept at 200 °C for 30 min. After cooling down to 65 °C in the same flow, the adsorption of O_2 was measured by exposing the catalyst to a flow of 21 vol% O_2/N_2 (20 mL min^{-1}) for 1 h. Finally, the catalyst was heated from 65 to 500 °C at a constant heating rate of 10 °C min^{-1} in a flow of He (60 mL min^{-1}). The desorption of O_2 was calculated from the signal of a TCD detector.

X-ray photoelectron spectroscopy (XPS) was employed to determine the Mn 2p, O 1s and C 1s binding energies of surface species of the as-prepared samples on a Thermo Scientific K-Alpha using Mg Ka radiation (1653.6 eV) at a beam power of 250 W. The binding energy of C1s (284.6 eV) was used as the internal standard.

2.3 Catalytic Activity Test

Catalytic tests were carried out on a fixed-bed quartz flow reactor with 50 mg catalyst (40–60 mesh). Typically, the catalysts were pretreated by 21 vol% O_2/N_2 at 300 °C for 1 h and then cooled down to 200 °C. The gas was switched to 10 vol% H_2/N_2 for 1 h at the temperature of 200 °C. Subsequently, the temperature was cooled down to 25 °C. Gaseous HCHO was generated by passing a by flowing 21% O_2/N_2 over the paraformaldehyde in a thermostatic water bath kept at 30 °C. The total flow rate through the reactor was remained at 30 mL min^{-1} and included 300 ppm HCHO, 21 vol% O_2 and N_2 equilibrium gas. The mass space velocity was 36,000 mL g_{cat}^{-1} h^{-1}. The analysis of the products was analyzed using a gas chromatograph equipped with hydrogen flame ionization detector (FID) and Ni catalyst convertor. No other carbon containing compounds except CO_2 in the products were detected for the tested catalyst. Thus HCHO conversion was calculated as follows:

$$\text{HCHO conversion } (\%) = \frac{[CO_2]_{out}}{[HCHO]_{in}} \times 100$$

Where $[CO_2]_{out}$ and $[HCHO]_{in}$ in the formula corresponds to the CO_2 concentration in the products and the concentration of HCHO in the gas flow, respectively.

3 Results and Discussion

3.1 Characterization of the Catalysts

3.1.1 N_2 Adsorption and Desorption

The N_2 adsorption and desorption isotherm of MnO_2-*r*, MnO_2-*n*, Ag/MnO_2-*r* and Ag/MnO_2-*n* are shown in Fig. 1. The results of the adsorption and desorption demonstrated that the all as-prepared samples performed the hysteresis phenomenon which was assigned to the type of IV isotherms [9]. The result indicated that mesoporous structure presented in the samples. After the addition of Ag into MnO_2-*r* and MnO_2-*n*, the hysteresis rings of Ag/MnO_2-*r* and Ag/MnO_2-*n* were smaller than that of MnO_2-*r* and MnO_2-*n*, perhaps due to the blockage of pores by Ag nanoparticles.

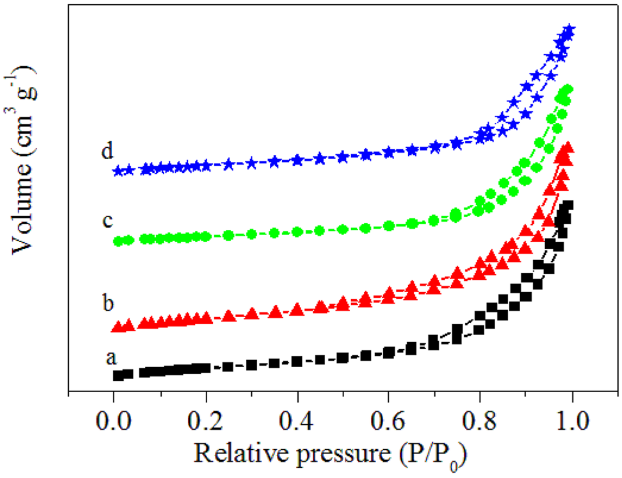

Fig. 1 N_2 adsorption and desorption isotherms of (a) MnO_2-*r*, (b) MnO_2-*n*, (c) Ag/MnO_2-*r* and (d) Ag/MnO_2-*n*

BET surface area and pore diameter as well as pore volume are summarized in Table 1. The surface areas of MnO_2-*r* and MnO_2-*n* were 102.1 and 119.7 m^2 g^{-1}, respectively. For Ag/MnO_2-*r* and Ag/MnO_2-*n*, the surface areas decreased to 71.2 and 76.1 m^2 g^{-1}, indicating that Ag nanoparticles formed on the surface with blocking pores of MnO_2-*r* and MnO_2-*n*. Meanwhile, the pore volume of MnO_2-*r* and MnO_2-*n* decreased in some extent, respectively, compared with those of MnO_2-*r* and MnO_2-*n*. The pore diameter and pore volume of Ag/MnO_2-*r* were 16.7 nm and 0.33 cm^3 g^{-1}, while the corresponding value of Ag/MnO_2-*n* were 14.2 nm and 0.36 cm^3 g^{-1}, respectively.

3.1.2 SEM and TEM Images

Figures 2 and 3 show SEM and TEM micrographs of the MnO_2-*n* and MnO_2-*r*, respectively. As can be clearly seen from Figs. 2a, b and 3a, the MnO_2-*n* derived from the water-bathing process was aggregated by a large number of sphere-like nanoparticles, which was consisted of many nanorods. The length of the rods was mostly 100–250 nm. From the Figs. 2c, d and 3b, it can be observed that MnO_2-*r* hydrothermally at 160 °C displayed a rod-like morphology, with the diameters of about 80 nm and lengths ranging from 2 to 5 μm. The morphology of MnO_2-*r* is in good agreement with that of the previously reported MnO_2 in the literatures [18, 21]. Therefore, the SEM and TEM results revealed that the morphology of the MnO_2 sample were strongly dependent on the preparation method and condition.

3.1.3 XRD Patterns

The XRD patterns of the MnO_2-*r*, MnO_2-*n*, Ag/MnO_2-*r* and Ag/MnO_2-*n* are shown in Fig. 4. It can be seen that the Fig. 4a, b could be well indexed to a pure tetragonal

Table 1 Pore structure and texture of the MnO_2-*r*, MnO_2-*n*, Ag/MnO_2-*r* and Ag/MnO_2-*n*

Catalyst	S_{BET} (m^2 g^{-1})	Pore diameter (nm)	Pore volume (cm^3 g^{-1})
MnO_2-*r*	102.1	13.4	0.37
MnO_2-*n*	119.7	11.9	0.40
Ag/MnO_2-*r*	71.2	16.7	0.33
Ag/MnO_2-*n*	76.1	14.2	0.36

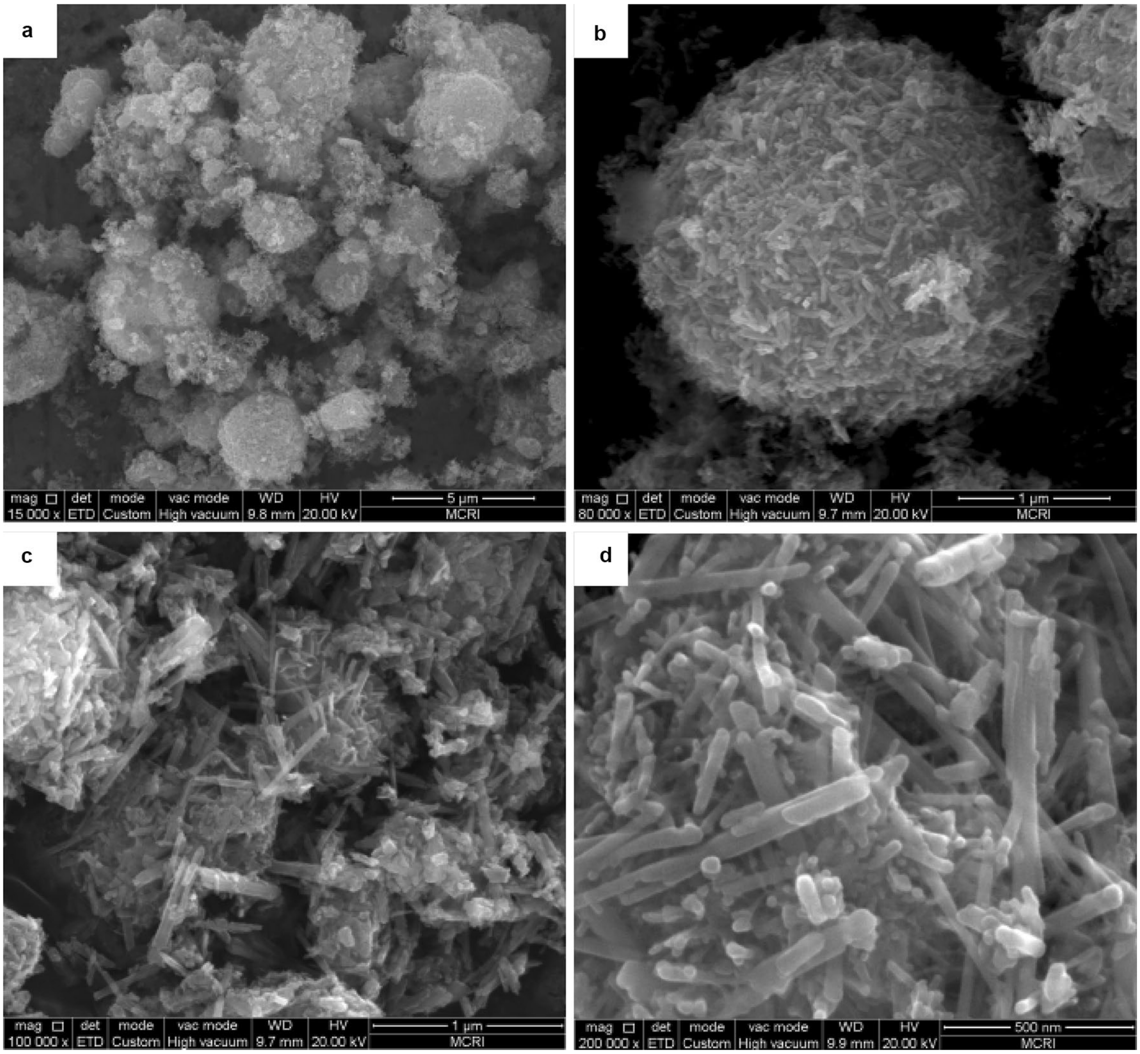

Fig. 2 SEM images of **a**, **b** MnO_2-*n* and **c**, **d** MnO_2-*r*

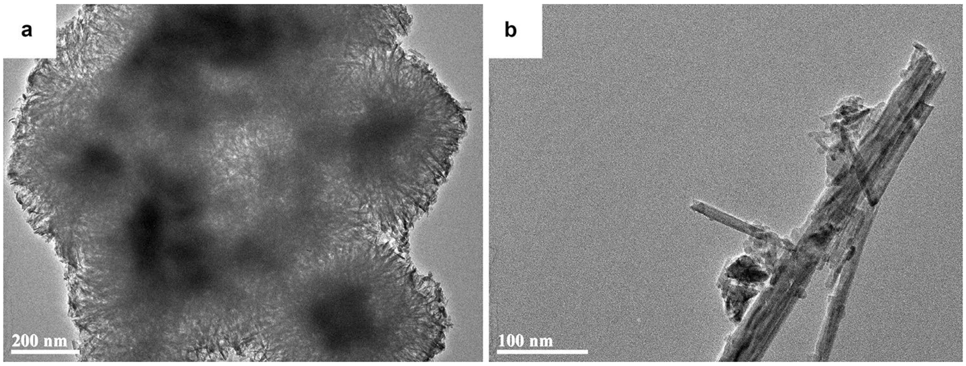

Fig. 3 TEM images of **a** MnO_2-*n* and **b** MnO_2-*r*

phase, which were in agreement with α-MnO_2 (JCPDS PDF 44-0141) [19]. The intensities of the diffraction peaks of the MnO_2-*r* were greatly lowered compared with those of MnO_2-*n*. The discrepancies in intensity of XRD peaks suggested the different in crystallinity of these two samples. As the addition of Ag into MnO_2-*r* or MnO_2-*n*, no Ag species (Ag^0, AgO) were observed in any samples, indicating that Ag species were highly dispersed on the MnO_2 support [14]. Meanwhile, it is found that the intensity of the diffraction peaks was weaker with the introduction of Ag.

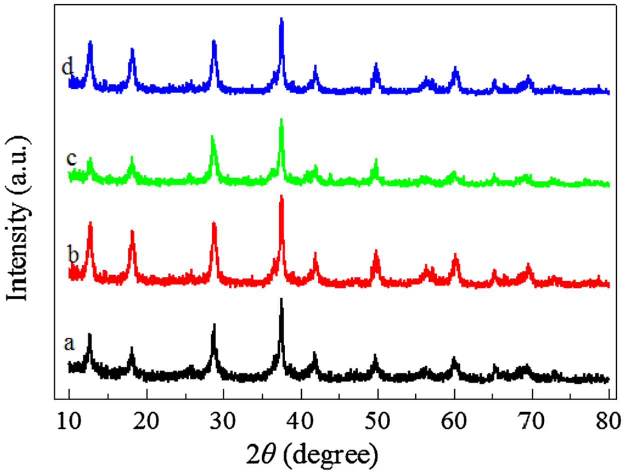

Fig. 4 XRD patterns of (a) MnO_2-*r*, (b) MnO_2-*n*, (c) Ag/MnO_2-*r* and (d) Ag/MnO_2-*n*

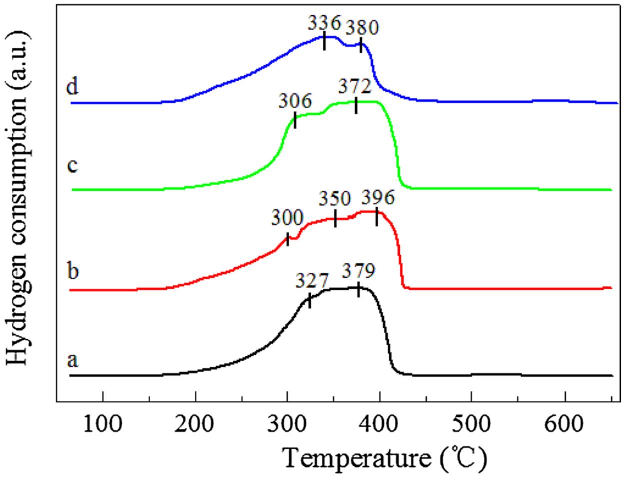

Fig. 5 H_2-TPR profiles of (a) MnO_2-*r*, (b) MnO_2-*n*, (c) Ag/MnO_2-*r* and (d) Ag/MnO_2-*n*

3.1.4 H_2-TPR

The H_2-TPR profiles of MnO_2-*r*, MnO_2-*n*, Ag/MnO_2-*r* and Ag/MnO_2-*n* are displayed in Fig. 5. Generally, it has reported that the reduction process of MnO_2 could be reasonably divided into two steps of MnO_2 to Mn_3O_4 and Mn_3O_4 to MnO [22]. For the case of MnO_2-*r*, there were two overlapped strong reduction peaks in the temperature range from 149 to 450 °C, which were observed at 327 and 379 °C. The assignment of the reduction peaks was not very clear, while they might correspond to the combined reduction of MnO_2/Mn_2O_3 into Mn_3O_4 and Mn_3O_4 to MnO. As can be seen in Fig. 5b, the MnO_2-*n* showed two overlapped reduction peaks at 149–450 °C with a slight shoulder at about 300 °C. It was possible to propose that the shoulder reduction peak of MnO_2-*n* was assigned to the readily reducible small cluster surface manganese species, which is in good accordance with the previous report by Tang et al. [10]. The two overlapped reduction peaks were similar to those of the MnO_2-*r* sample. It is clearly found that the reduction temperatures of MnO_2-*n* shifted to higher regions in comparison with those of MnO_2-*r*, implying that the morphology of MnO_2 dramatically influenced on the reduction behavior. Similar phenomenon has been reported by Li et al. [23].

After addition of Ag, the two reduction peaks centered at around 306 and 327 °C for Ag/MnO_2-*r* the shifted to lower temperature region, indicating the occurrence of metal-support interaction between Ag and MnO_2-*r*. This phenomenon is often interpreted in terms of the activation and spillover of hydrogen from the initially reduced silver to manganese oxides, and consequently promoted their reductions [24–26]. It has also reported that the presence of silver could promote the reducibility of surface oxygen on CeO_2 and induce the oxygen transfer during the reduction process [27]. Thus, the reduction peaks of Ag/MnO_2-*r* could be ascribed to the simultaneous reduction of dispersed Ag_2O to Ag and MnO_2 to MnO. The H_2-TPR of Ag/MnO_2-*n* exhibited one intensive reduction peak at about 336 °C with a weak shoulder peak at around 380 °C. It is obviously observed that the introduction of Ag into Ag/MnO_2-*n* improved the reducibility, which was similar to that of Ag/MnO_2-*r*. Therefore, the H_2-TPR results indicated that the reduction of the four samples enhanced in the order of MnO_2-*n* < MnO_2-*r* < Ag/MnO_2-*n* < Ag/MnO_2-*r*, in according to that of catalytic activities.

3.1.5 O_2-TPD

O_2-TPD experiments were performed over the MnO_2-*r*, MnO_2-*n*, Ag/MnO_2-*r* and Ag/MnO_2-*n*, and the profiles are shown in Fig. 6. In general, the desorption oxygen species of the oxide followed the sequence of oxygen molecule (O_2) > oxygen molecule anion (O_2^-)>oxygen anion (O^-)>lattice oxygen (O^{2-}) [28, 29]. The desorption of O_2 might occur at very low temperature (< 200 °C), while the surface active oxygen species such as O_2^- and O^- would desorb between 200 and 400 °C, and the lattice oxygen from MnO_2 could desorb above 400 °C [29]. As displayed in Fig. 6a, there was only one broad O_2 desorption peak presented on the MnO_2-*r* sample in the temperature range of 150 to 350 °C and the peak was centered at 236 °C, which could be attributed to the desorption of O_2, O_2^- and O^-. For the case of MnO_2-*n*, one strong O_2 desorption peak located at 368 °C along with a weak broad peak centered at 243 were observed, which might be ascribed to the desorption of O_2^- and O^-, respectively. Therefore, the desorption temperature of O_2 greatly depended on the morphology of MnO_2-*r* and MnO_2-*n*.

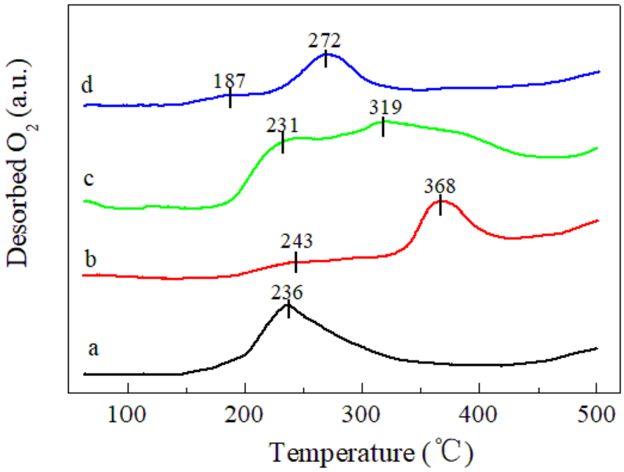

Fig. 6 O_2-TPD profiles of (a) MnO_2-*r*, (b) MnO_2-*n*, (c) Ag/MnO_2-*r* and (d) Ag/MnO_2-*n*

As shown in Fig. 6c, after introduction of Ag into MnO_2-*r*, it is noted that a significant increase of the desorption peaks in the range of 175 and 400 °C were observed for Ag/MnO_2-*r*. It can be found two overlapped desorption peak, located at 231 and 319 °C, which was lower than that of MnO_2-*r*. This data suggested that the presence of Ag could be beneficial to produce surface active oxygen in the Ag/MnO_2-*r* catalyst. Similar phenomena were also occurred on the Ag/MnO_2-*n*. Obviously, the weak broad peak shifted to 187 °C and the strong peak shifted to 272 °C, which were lower to 56 and 96 °C than those of MnO_2-*n*. These results indicated that the introduction of Ag would facilitate to generate much more oxygen desorption during the O_2-TPD process. Wang et al. [30] investigated that the presence of Pt dramatically decreased the desorption temperature of O_2 and elevated chemical adsorption of O_2 (O_2^- and O^-) as well as the excellent mobility of lattice oxygen, which greatly facilitated the enhancement on catalytic oxidation activity. Ma et al. [31] reported that Au nanoparticles promoted desorption of the surface oxygen species and the catalyst exhibited a higher activity for the HCHO oxidation. So, the enhanced activation of chemisorbed oxygen by Ag addition should be greatly responsible for the outstanding activity of Ag/MnO_2-*r* and Ag/MnO_2-*n* (see Fig. 8).

Compared with Fig. 6c, d, the O_2 desorption peak area of Ag/MnO_2-*r* was larger than that of Ag/MnO_2-*n*, indicating Ag/MnO_2-*r* had abundant surface active oxygen species. Generally speaking, surface active oxygen species might offer a higher catalytic activity in oxidation reactions [9, 31]. This phenomenon probably attributed to the lattice defect and oxygen vacancy that resulted from nanorod structure of the MnO_2-*r* sample. It is beneficial for oxygen in the gas phase to be activated and adsorb onto the MnO_2-*r* surface. Therefore, Ag/MnO_2-*r* performed the highest O_2 mobility and best catalytic ability, in accordance with the result of catalytic activity (Fig. 8).

3.1.6 XPS

XPS spectra of MnO_2-*r*, MnO_2-*n*, Ag/MnO_2-*r* and Ag/MnO_2-*n* were measured to probe the states of the surface Ag, Mn and O element, as displayed in Fig. 7.

The Ag 3d XPS spectra of the Ag/MnO_2-*r* and Ag/MnO_2-*n* catalysts are shown in Fig. 7a. It has been reported that Ag 3d possessed signals at 368.0 and 375.0 eV [32, 33], which were ascribed to the escape of electrons from the $3d_{5/2}$ and $3d_{3/2}$ core levels, respectively. Following the previous assignments [13, 34], the Ag $3d_{5/2}$ had two components at 368.0 and 367.5 eV. The former indicated the presence of Ag^0, whereas the later could be reasonably attributed to Ag_2O. However, these Ag or Ag_2O species could not be apparently detected by XPS in Fig. 7a, probably because of the small loading content (0.1 wt % Ag in the Ag/MnO_2-*r* and Ag/MnO_2-*n* catalysts). Generally speaking, Ag_2O could be decomposed completely into metallic Ag and O_2 when calcined at temperatures higher than 400 °C in air [10]. In addition, Weaver et al. [35] had discovered incomplete dissociation of Ag_2O, which was calcined at 300 °C, generating a combination of both Ag_2O and Ag states on the surface of catalysts. In our situation, both Ag/MnO_2-*r* and Ag/MnO_2-*n* catalysts were treated at 300 °C for 1 h by 21 vol% O_2/N_2. Therefore, it can be speculated that both metallic Ag and Ag_2O were formed on Ag/MnO_2-*r* and Ag/MnO_2-*n* catalyst surface. As for the supports of MnO_x-CeO_2 or CeO_2 [10, 34], it has been also found that the active oxygen species on the surface of CeO_2 or MnO_x–CeO_2 could be transferred to Ag and oxidized it into Ag^+, due to the strong interaction between Ag and supports. Similarly, it is possible that the electron charge transfer from Ag to MnO_2 would readily cause the formation of positively charged Ag^+ clusters in our case.

In the Mn 2p spectra (Fig. 7b), two clear peaks were discovered and implied the identical chemical state of Mn atoms in the all as-prepared samples. For the MnO_2-*r* and MnO_2-*n*, the splitting energy of the Mn 2p peak (11.8 eV) approached that of Mn^{4+}, in according with the energy separation between Mn $2p_{3/2}$ and Mn $2p_{1/2}$ reported previously [24]. Moreover, after addition of Ag into MnO_2-*r* and MnO_2-*n*, obvious upshift of the Mn $2p_{3/2}$ and Mn $2p_{1/2}$ occurred, which indicated that the addition of Ag increased Mn^{4+} ions. In special, the main manganese in the Ag/MnO_2-*r* was Mn^{4+}. Tang et al. [10] reported that more Mn^{4+} species resulted in much higher catalytic activity for the complete oxidation of HCHO over MnO_x-CeO_2 catalyst.

As shown in Fig. 7c, two surface oxygen species could be apparently found in the O 1s spectra. For the sample of MnO_2-*r*, the component centering at 532.3 eV indicated the

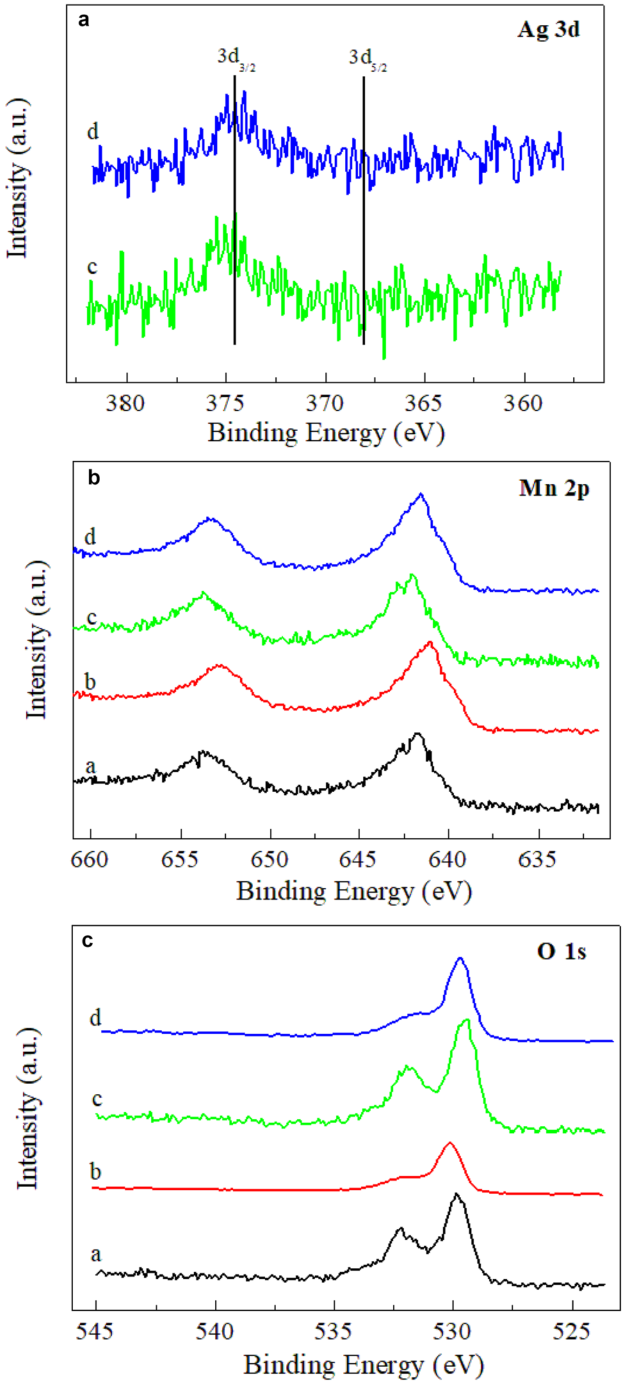

Fig. 7 XPS spectra of (a) MnO_2-*r*, (b) MnO_2-*n*, (c) Ag/MnO_2-*r* and (d) Ag/MnO_2-*n*. **a** Ag 3d, **b** Mn 2p and **c** O 1s

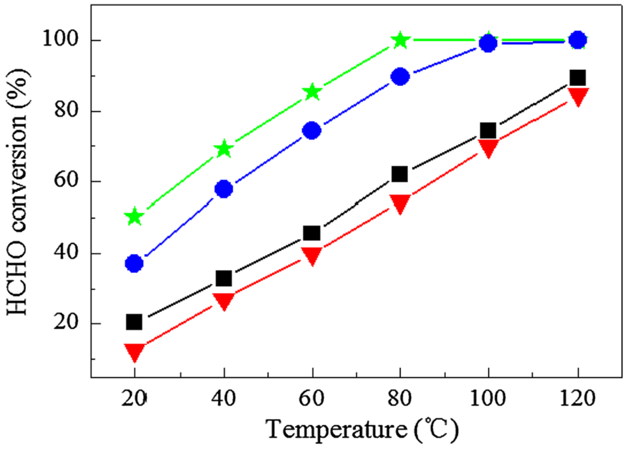

Fig. 8 HCHO conversion over (filled square) MnO_2-*r*, (filled inverted triangle) MnO_2-*n*, (filled five pointed triangle) Ag/MnO_2-*r* and (filled circle) Ag/MnO_2-*n*. Reaction conditions: 300 ppm HCHO, 21 vol % O_2 and N_2 (balance). The total flow rate and WHSV are 30 mL min^{-1} and 36,000 mL g_{cat}^{-1} h^{-1}, respectively

presence of adsorbed oxygen or surface hydroxyl species, and the component locating at 529.9 eV might be reasonably ascribed to surface oxygen atoms, following the previous assignments [15]. It has observed that a slight shift to higher binding energy for MnO_2-*r* than the MnO_2-*n*. As the introduction of Ag into MnO_2-*r* and MnO_2-*n*, a discernible shift to lower binding energy for Ag/MnO_2-*r* and Ag/MnO_2-*n* was observed in comparison to MnO_2-*r* and MnO_2-*n*, due to an increase of their negative charge [36]. It is clearly observed that the intensity of higher BE (531.9 eV) of the Ag/MnO_2-*r* catalyst performed strongest, implying more surface active oxygen. The result is well in agreement with the O_2-TPD analysis (Fig. 6). It has been reported that more surface adsorbed oxygen and hydroxyl species played a crucial role to promote the catalytic activity for HCHO oxidation [13]. Therefore, it can speculate that the Ag/MnO_2-*r* would possess excellent catalytic performance for the HCHO oxidation, in accordance to the result of catalytic test (see Fig. 8).

3.2 Catalytic Activity

Figure 8 shows the catalytic activities of MnO_2-*r*, MnO_2-*n*, Ag/MnO_2-*r* and Ag/MnO_2-*n* in terms of HCHO conversion as a function of reaction temperature. Obviously, MnO_2-*r* and MnO_2-*n* performed very low HCHO conversion in the temperature range investigated. They obtained only 89.7% and 84.2% conversion of HCHO at 120 °C, respectively. The result indicated that the temperature dependence of HCHO conversion was significantly related to their morphologies. The MnO_2 with the morphology of nanorods exhibited better catalytic activity for the HCHO oxidation in comparison with that of MnO_2 nanoparticles. Similar result was also found by Shi et al. [18], who observed that rod-like MnO_2 showed highest catalytic performance than that of flower-like MnO_2 and dumbbell-like MnO_2 for the combustion of toluene. As the addition of Ag to MnO_2-*r* and MnO_2-*n*, complete HCHO conversion was achieved at the temperature of 80 and 100 °C, respectively. Especially,

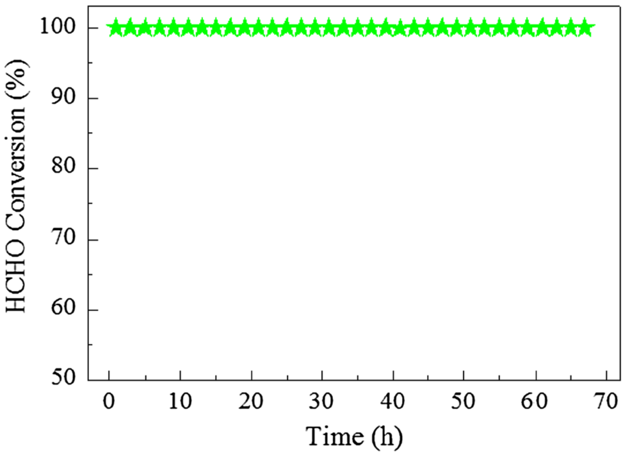

Fig. 9 Stability test of the Ag/MnO_2-*r* catalyst at 80 °C with the reaction condition of 300 ppm HCHO, 21 vol % O_2 and N_2 (balance)

the Ag/MnO_2-*r* exhibited outstanding catalytic activity for the oxidation of HCHO.

Figure 9 shows the stability test of the Ag/MnO_2-*r* catalyst at 80 °C with the reaction condition of 300 ppm HCHO, 21 vol % O_2 and N_2 (balance). It can be found that the Ag/MnO_2-*r* catalyst performed good stability, which kept the 100% conversion of HCHO during 67 h.

The results above demonstrated that the morphology of nano-MnO_2 samples played an important role on their physicochemical properties, thus leading to the different synergy effect between Ag and MnO_2. The Ag/MnO_2-*r* catalyst displayed stronger synergy than Ag/MnO_2-*n*. The strong synergy could be beneficial for the reducibility of manganese oxides through the spillover of hydrogen, increase HCHO adsorption ability of MnO_2 and generate more lattice oxygen species [37]. In turn, the reaction activity could be influenced accordingly, as revealed from the result of catalytic activity study. It is well known that oxygen vacancy and reducibility of a transition metal oxide were crucial factors impacting its catalytic activity [10, 23]. The existence of oxygen vacancies promoted the activation of oxygen molecules to active oxygen species. A good reducibility of the catalyst might offer a facile redox process that would lead to an enhanced catalytic performance [17]. As found from the H_2-TPR and O_2-TPD studies, the Ag/MnO_2-*r* possessed better low-temperature reducibility and higher active oxygen species concentrations (relevant to the surface oxygen vacancy densities) than Ag/MnO_2-*n*, in good agreement with their catalytic activity sequence. Hence, it can be deduced that the better low-temperature reducibility and higher active oxygen species concentrations mainly contributed to high catalytic performance of the Ag/MnO_2-*r* for the HCHO oxidation.

4 Conclusions

The MnO_2 nanorods (MnO_2-*r*) and MnO_2 nanoparticles (MnO_2-*n*) were synthesized by the hydrothermal route and water-bathing method, respectively. As the addition of Ag, the Ag/MnO_2-*r* catalyst performed superior catalytic activity for the HCHO oxidation, which gained 100% HCHO conversion at 80 °C. It has been observed that the morphology of MnO_2 significantly influenced on the properties of the catalysts. Among the as-prepared samples, Ag/MnO_2-*r* possessed easy reducibility and active surface oxygen, which was mainly contributed to the high activity for HCHO oxidation. Moreover, the Ag/MnO_2-*r* catalyst performed good stability. Thus, it is a promising catalyst for the catalytic oxidation of HCHO, because of its low-cost, high activity and stability.

Acknowledgements This work was sponsored financially by the postgraduate' Innovative Entrepreneurial Training Program of Xi'an Shiyou University (Nos. YCS18111006 and YCS18211014) and the college student' Innovative Entrepreneurial Training Program of nation (201810705017), the Science & Technology Plan Project of Xi'an City (No. 2017081CG/RC044 (XASY006)), Young Talent fund of University Association for Science and Technology in Shaanxi (20180604) and the National Nature Science Foundation of China (No. 21606177).

References

1. Bai BY, Qiao Q, Li JH, Hao JM (2016) Progress in research on catalysts for catalytic oxidation of formaldehyde. Chin J Catal 37:102–122
2. Zhang CB, Liu FD, Zhai YP, Ariga H, Yi N, Liu YC, Asakura K, Flytzani-Stephanopoulos M, He H (2012) Alkali-metal-promoted Pt/TiO_2 opens a more efficient pathway to formaldehyde oxidation at ambient temperatures. Angew Chem Int Ed 51:9628–9632
3. Zhang ZX, Jiang Z, Shangguan WF (2016) Low-temperature catalysis for VOCs removal in technology and application: a state-of-the-art review. Catal Today 264:270–278
4. Nie LH, Yu JG, Jaroniec M, Tao FF (2016) Room-temperature catalytic oxidation of formaldehyde on catalysts. Catal Sci Technol 6:3649–3669
5. Yang TF, Huo Y, Liu Y, Rui ZB, Ji HB (2017) Efficient formaldehyde oxidation over nickel hydroxide promoted $Pt/\gamma\text{-}Al_2O_3$ with a low Pt content. Appl Catal B 200:543–551
6. Zhang CB, Li YB, Wang YF, He H (2014) Sodium-promoted Pd/TiO_2 for catalytic oxidation of formaldehyde at ambient temperature. Environ Sci Technol 48:5816–5822
7. Chen BB, Zhu XB, Wang YD, Yu LM, Lu JQ, Shi C (2017) Nano-sized gold particles dispersed on HZSM-5 and SiO_2 substrates for catalytic oxidation of HCHO. Catal Today 281:512–519
8. Wang JL, Li JG, Jiang CJ, Zhou P, Zhang PY, Yu JG (2017) The effect of manganese vacancy in birnessite-type MnO_2 on room-temperature oxidation of formaldehyde in air. Appl Catal B 204:147–155
9. Bai BY, Arandiyan H, Li JH (2013) Comparison of the performance for oxidation of formaldehyde on nano-Co_3O_4, 2D-Co_3O_4, and 3D-Co_3O_4 catalysts. Appl Catal B 142–143:677–683

10. Tang XF, Li YG, Huang XM, Xu YD, Zhu HQ, Wang JG, Shen WJ (2006) MnO_x-CeO_2 mixed oxide catalysts for complete oxidation of formaldehyde: effect of preparation method and calcination temperature. Appl Catal B 62:265–273
11. Nie LH, Wang J, Yu JG (2017) Preparation of a Pt/TiO_2/cotton fiber composite catalyst with low air resistance for efficient formaldehyde oxidation at room temperature. RSC Adv 7:21389–21397
12. Yan ZX, Xu ZH, Cheng B, Jiang CJ (2017) Co_3O_4 nanorod-supported Pt with enhanced performance for catalytic HCHO oxidation at room temperature. Appl Surf Sci 404:426–434
13. Bai BY, Li JH (2014) Positive effects of K^+ ions on three-dimensional mesoporous Ag/Co_3O_4 catalyst for HCHO oxidation. ACS Catal 4:2753–2762
14. Ma L, Wang DS, Li JH, Bai BY, Fu LX, Li YD (2014) Ag/CeO_2 nanospheres: efficient catalysts for formaldehyde oxidation. Appl Catal B 148–149:36–43
15. Lu L, Tian H, He JH, Yang QW (2016) Graphene-MnO_2 hybrid nanostructure as a new catalyst for formaldehyde oxidation. J Phys Chem C 120:23660–23668
16. Bai BY, Qiao Q, Li JH, Hao JM (2016) Synthesis of three-dimensional ordered mesoporous MnO_2 and its catalytic performance in formaldehyde oxidation. Chin J Catal 37:27–31
17. Averlant R, Royer S, Giraudon JM, Bellat JP, Bezverkhyy I, Weber G, Lamonier JF (2014) Mesoporous silica-confined manganese oxide nanoparticles as highly efficient catalysts for the low-temperature elimination of formaldehyde. ChemCatChem 6:152–161
18. Shi FJ, Wang F, Dai HX, Dai JX, Deng JG, Liu YX, Bai GM, Ji KM, Au CT (2012) Rod-, flower-, and dumbbell-like MnO_2: highly active catalysts for the combustion of toluene. Appl Catal A 433–434:206–213
19. Liang SH, Teng F, Bulgan G, Zong RL, Zhu YF (2008) Effect of phase structure of MnO_2 nanorod catalyst on the activity for CO oxidation. J Phys Chem C 112:5307–5315
20. Li BX, Rong GX, Xie Y, Huang LF, Feng CQ (2006) Low-temperature synthesis of α-MnO_2 hollow urchins and their application in rechargeable Li^+ batteries. Inorg Chem 45:6404–6410
21. Zhou J, Qin LF, Xiao W, Zeng C, Li N, Lv T, Zhu H (2017) Oriented growth of layered-MnO_2 nanosheets over α-MnO_2 nanotubes for enhanced room-temperature HCHO oxidation. Appl Catal B 207:233–243
22. Torres JQ, Giraudon JM, Lamonier JF (2011) Formaldehyde total oxidation over mesoporous MnO_x catalysts. Catal Today 176:277–280
23. Li JM, Qu ZP, Qin Y, Wang H (2016) Effect of MnO_2 morphology on the catalytic oxidation of toluene over Ag/MnO_2 catalysts. Appl Surf Sci 385:234–240
24. Tang XF, Chen JL, Li YG, Li Y, Xu YD, Shen WJ (2006) Complete oxidation of formaldehyde over Ag/$MnOx$-CeO_2 catalysts. Chem Eng J 118:119–125
25. Gong DD, Li SS, Guo SX, Tang HG, Wang H, Liu Y (2018) Lanthanum and cerium Co-modified Ni/SiO_2 catalyst for CO methanation from syngas. Appl Surf Sci 434:351–364
26. Li SS, Gong DD, Tang HG, Ma Z, Liu ZT, Liu Y (2018) Preparation of bimetallic Ni@Ru nanoparticles supported on SiO_2 and their catalytic performance for CO methanation. Chem Eng J 334:2167–2178
27. Kang Y, Sun M, Li A (2012) Studies of the catalytic oxidation of CO over Ag/CeO_2 catalyst. Catal Lett 142:1498–1504
28. Cai T, Huang H, Deng W, Dai QG, Liu W, Wang XY (2015) Catalytic combustion of 1,2-dichlorobenzene at low temperature over Mn-modified Co_3O_4 catalysts. Appl Catal B 166–167:393–405
29. Huang H, Dai QG, Wang XY (2014) Morphology effect of Ru/CeO_2 catalysts for the catalytic combustion of chlorobenzene. Appl Catal B 158–159:96–105
30. Wang M, Zhang LX, Huang WM, Zhou YJ, Zhao H, Lv J, Tian JJ, Kan XT, Shi JL (2017) Pt/MnO_2 nanosheets: facile synthesis and highly efficient catalyst for ethylene oxidation at low temperature. RSC Adv 7:14809–14815
31. Ma CY, Wang DH, Xue WJ, Dou BJ, Wang HL, Hao ZP (2011) Investigation of formaldehyde oxidation over Co_3O_4–CeO_2 and Au/Co_3O_4–CeO_2 catalysts at room temperature: effective removal and determination of reaction mechanism. Environ Sci Technol 45:3628–3634
32. Li DD, Yang GL, Li PL, Wang HL, Zhang PY (2016) Promotion of formaldehyde oxidation over Ag catalyst by Fe doped MnO_x support at room temperature. Catal Today 277:257–265
33. Qu ZP, Chen D, Sun YH, Wang Y (2014) High catalytic activity for formaldehyde oxidation of AgCo/APTES@MCM-41 prepared by two steps method. Appl Catal A 487:100–109
34. Ma L, Seo CY, Chen XY, Li JH, Schwank JW (2018) Sodium-promoted Ag/CeO_2 nanospheres for catalytic oxidation of formaldehyde. Chem Eng J 350:419–428
35. Weaver JF, Hoflund GB (1994) Surface characterization study of the thermal decomposition of AgO. J Phys Chem 98:8519–8524
36. Hu PP, Amghouz Z, Huang ZW, Xu F, Chen YX, Tang XF (2015) Surface-confined atomic silver centers catalyzing formaldehyde oxidation. Environ Sci Technol 49:2384–2390
37. Shi FJ, Wang F, Dai HX, Dai JX, Deng JG, Liu YX, Bai GM, Ji KM, Au CT (2012) Rod-, flower-, and dumbbell-like MnO_2: highly active catalysts for the combustion of toluene. Appl Catal A 433–34:206–213